Modeling and validating a SuperDARN radar's power density profile

G. W. Perry[1], K. D. Ruzic[2], K. Sterne[3], A. D. Howarth[2] and A. W. Yau[2]

[1]Center for Solar-Terrestrial Research, New Jersey Institute of Technology

[2]Department of Physics and Astronomy, University of Calgary.

[3]The Bradley Department of Electrical and Computer Engineering, Virginia Polytechnic Institute and State University.

Corresponding author: Gareth Perry gperry@njit.edu

Key Points:

- SuperDARN Saskatoon's power density profile is modeled in an empirical ionosphere
- A simulated power density profile is validated with the e-POP RRI instrument
- The power density model is a useful tool for studying High Frequency radio wave propagation

Abstract

We have developed a model that simulates the power density profile of the Saskatoon Super Dual Auroral Radar Network (SuperDARN) radar at ionospheric altitudes. The model uses ray tracing software to project the radar system's vacuum power profile to ionospheric altitudes, taking into account the influence of the ionospheric medium on the propagation characteristics of the High Frequency radio waves. Measurements of the radar's transmissions by the Radio Receiver Instrument (RRI) in low-Earth orbit are used to validate the model during five experiments which occurred between August 4-8, 2017. Comparisons between simulated and measured RRI antenna voltages show good agreement, although there are clear instances in which the model underperforms. Nevertheless, the model demonstrates its utility as a tool for interpreting several RRI measurements of SuperDARN radars. The model also helps address a lack of knowledge of a SuperDARN radar's power profile at ionospheric altitudes. In particular, we assess the assumption that SuperDARN's scattering volume lies along the great-circle path of the transmitting beam's bearing. Comparisons between the model and RRI's measurements show that this assumption is reasonable for the five experiments investigated in this work. The model presents a new way of carrying out SuperDARN and HF radio science investigations.

Plain Language Summary

The Super Dual Auroral Radar Network (SuperDARN) radar system located in Saskatoon, Canada is a powerful tool for studying the high-latitude ionosphere. Despite the fact that the system has been operating nearly continuously since 1993, there is very little understanding of what the radar's power profile looks like at ionospheric altitudes where its radar echoes originate. This is simply due to a lack of available measurements. As a result, it is customary to simply assume that the radar's power profile at ionospheric altitudes resembles that of its power profile in a vacuum projected along great-circle trajectories up to ionospheric altitudes. This assumption is limited because it does not adequately account for the fact that the radar's power profile can be influenced by the ionospheric medium in which it is immersed. In this work, we have developed a model of SuperDARN Saskatoon's power profile at ionospheric altitudes which properly accounts for the influence of the ionosphere. Furthermore, we have compared the model's output to several measurements of the Saskatoon radar made by a radio receiver in low-Earth orbit to validate the model. Our results show that the model is accurate and can be used as a useful tool for studying SuperDARN's power profile at ionospheric altitudes.

1 Introduction

1.1 Background and Motivation

The Super Dual Auroral Radar Network (Chisham et al., 2007), a globally distributed network of High Frequency (HF; 3-30 MHz) radars, monitors plasma density irregularities in the high-latitude ionosphere. The irregularities drift at the local plasma convection velocity (Villain et al., 1985; Ruohoniemi, 1987). Doppler velocity measurements of the irregularities from multiple SuperDARN systems are then combined to deduce high-latitude plasma convection flows and the large-scale electric fields that drive them (Ruohoniemi & Baker, 1998; Bristow et al., 2016). These fields are generated as a result of complex magnetosphere-ionosphere-thermosphere (MIT) coupling processes. As such, SuperDARN is a vital remote sensing tool for undertstanding complex plasma interactions in the near-Earth geospace environment.

The SuperDARN technique relies on coherent backscatter generated by ionospheric irregularities to detect and measure the bulk velocity of the ionospheric plasma. The generally accepted theory of HF radar backscatter requires that two conditions must be satisfied (Milan et al., 1997a). First, plasma density irregularities must be present in the scattering volume. Second, the incident radio wave must satisfy the Bragg condition at that location. At the decameter scale, the wavelength of SuperDARN transmissions, cross-field plasma diffusion (with respect to the magnetic field) is much slower than parallel diffusion (Tsunoda, 1988). F-region plasma density irregularities are strongly field-aligned (hence the name field-aligned-irregularities; FAIs) with the normal of wavevectors that are orthogonal to the magnetic field. Therefore, to satisfy the Bragg condition, an incident radio wave must have an aspect angle that is close to orthogonal with the magnetic field. This is commonly referred to as the "aspect angle condition".

Geolocating a radar echo is an important problem in HF remote sensing systems, including SuperDARN. A key assumption made in SuperDARN geolocation algorithms is that the scattering volume where the aspect angle condition is satisfied is located along the great-circle path trajectory of the transmitting beam – along the radar's main lobe. There is ample evidence that this may not always be true. For example, echoes originating from secondary maxima in a SuperDARN radar's power profiles are common (Milan et al., 1997b; Burrell et al., 2015, 2018). Furthermore, MIT coupling processes can generate large scale plasma density irregularities along the transmission trajectory paths which can deflect HF transmissions laterally from their nominal great-circle path trajectories. Observations of these deflections were reported by Perry et al., (2016) and Warrington et al. (1997). In general, the validity and applicability of the assumption under various geomagnetic conditions is not well understood. The limitations of SuperDARN geolocation algorithms are well documented (cf. Chisham et al., 2008; Yeoman et al., 2008), attesting to the challenge of HF radar echo geolocation problem.

One course of action for improving SuperDARN's geolocation algorithms is to model the system's power density profile at ionospheric altitudes with ray tracing techniques to narrow down the location of the scattering volume. This would address to key factors in the SuperDARN backscattering process (assuming FAIs are present): the ray paths of radio waves incident on the scattering volume and their power density. Accordingly, in this work, we present a model of the power density profile of the SuperDARN Saskatoon radar propagated into the F-region ionosphere. We then validate the model using data collected during conjunctions between the radar and the Radio Receiver Instrument (RRI; James et al., 2015) onboard the Cascade, Smallsat and Ionospheric Polar Explorer (CASSIOPE; Yau et al., 2015) spacecraft.

The model has two purposes. First, it can be used to address a gap in knowledge of SuperDARN's power density profile at ionospheric altitudes to improve our understanding of how the system operates, the coherent backscatter mechanism, and improve our ability to probe the MIT system using HF radio techniques. In particular we explore the assumption that the main lobe of SuperDARN's power density profile follows a great-circle path. Second, the model can be used as a tool for interpreting measurements of SuperDARN transmissions acquired in low-Earth orbit, to help distinguish variations in the received signal that are a feature of the radar's power profile from those that may be due to geophysical phenomena.

1.1 Previous HF Ray Trace Modeling Work

Historically, SuperDARN-related modeling efforts have focused on HF ray paths and determining where the rays satisfy the aspect angle condition (e.g., André, et al. 1997; Michael et al., 2020). One advantage of this technique is that it does not require one to simulate plasma density irregularities – it is assumed that irregularities are present everywhere, yet it is effective enough to provide context to radar data and facilitate the design and deployment of new systems. The technique is also consistent with existing SuperDARN geolocation algorithms in that it does not consider the radar's power profile, only the geometry of the backscattering process.

In an effort to better understand SuperDARN velocity data, Ponomarenko et al. (2009) developed a model for simulating radar echo returns generated by FAIs. Their sophisticated model considered a backscatter cross-section, higher-order corrections to the aspect angle condition, and geometric optics effects, but did not take the power profile of the simulated radar into account. Nevertheless, their model enabled quantitative diagnoses of SuperDARN backscatter characteristics.

In preparation for RRI science operations, Gillies et al. (2010) used ray tracing to predict the relative O- and X-mode power profile for the SuperDARN radars located at Saskatoon, Prince George, and Rankin Inlet. Their ray trace modeling considered the polarization state of the transmitted signal along the ray path. It also accounted for the initial polarization state of the signal at the selected radar. It did not account for the absolute power profile of the radars; the authors assumed an isotropic radiator, a suitable simplification considering that the relative power between the propagation modes was the quantity of interest. The work predicted that the majority of SuperDARN's power should be dominated by the X-mode north of the modeled radars, with a latitudinally narrow "X-mode only" feature prominent at CASSIOPE altitudes during times in which the ionosphere's peak frequency is low. Neither prediction has been tested in SuperDARN-RRI experiments.

Seminal work by Warrington et al. (2012) on studying the influence of large-scale plasma density structures on HF radio wave propagation conditions in the high-latitude ionosphere included a ray trace modeling effort which used ray density as a proxy for signal strength. The authors noted that transmitter radiation patterns could be specified when necessary. Their model was able to accurately reproduce data collected between transmitter-receiver pairs in high-latitude regions that exhibited dramatic angle of arrival deviations attributed to pronounced plasma density perturbations along the intervening ray paths.

An accurate representation of a transmitter's gain pattern is critical to computing its power profile. Models of some SuperDARN gain patterns exist (e.g., Milan et al., 1997a; Sterne et al., 2011); however, they only show the far field radiation pattern in a vacuum. In this work, we are interested in SuperDARN Saskatoon's power density profile at ionospheric altitudes. One could conceivably model the radiation pattern of a radar at all altitudes of interest by using great-circle paths to project a radar's gain pattern into the ionosphere. However, the pattern would only be appropriate for operating frequencies that are well above the ionosphere's critical frequency – when the index of refraction of the propagating radio waves is close to unity. Otherwise, the pattern would be distorted by vertical and horizontal refraction.

We report on the creation and validation of a model of a SuperDARN radar's power density profile, taking into account the influence of the ionospheric medium. This work is motivated by Perry et al. (2016), who detected significant deviations in SuperDARN's power profile with RRI in the high-latitude ionosphere. They could not conclusively attribute the deviations to large scale plasma density irregularities along the ray path since the expected power profile of a SuperDARN radar at ionospheric altitudes was not well understood. This work is a first step towards gaining new insight into Perry et al. (2016)'s observations and using RRI to gain new insight into the effects of ionospheric irregularities at high-latitudes and their effects on HF radio wave propagation.

In the next section, Section 2, we will describe how the model is created by using the provision of high-frequency raytracing laboratory for propagation studies (PHaRLAP; hereafter referred to as Pharlap) ray trace toolbox (Cervera and Harris, 2014) to propagate a modeled SuperDARN far field radiation pattern through an empirical model of the ionosphere provided by the International Reference Ionosphere (IRI) (Bilitza et al., 2008). In Section 3, we will show predictions of SuperDARN power density maps in the geographic region around Saskatoon and then validate the maps with RRI measurements. We will focus on the SuperDARN Saskatoon radar located due to the availability of measurements of that system's transmissions from ionospheric altitudes. In Section 4 we will discuss the results of the validation efforts and discuss how the model output can help improve our understanding of HF radio wave propagation in the region. Finally, in Section 5, we will summarize our work and outline future developments of the model.

2 Methodology

2.1 SuperDARN Saskatoon

In this work we are focused on the power profile of the SuperDARN radar at Saskatoon, Saskatchewan, Canada (52.16° N, 106.53° W, geographic), which has been in operation since 1993. The radar (like all SuperDARN radars) uses electronic beam steering techniques to direct its main lobe in 16 directions, referred to as "beams", separated by 3.24° in bearing. The radar's boresight, the bearing of antenna array's front main lobe, is at 23.1° (east of geographic north), and marks the shared border of Beams 7 and 8 (using the 0-15 beam numbering scheme in which the beam numbers increase in a clockwise direction). It is important to note that the radar does not usually transmit along the boresight, but along its numbered beams. Thus, as we will see, Beam 7, which is usually regarded as the "central beam", has a bearing of 21.48°, not 23.1°.

Figure 1 shows two polar plots of the modeled gain pattern (also commonly referred to as the radiation pattern) of the SuperDARN Saskatoon radar transmitting on Beam 7 at 11.2 MHz. This gain pattern was produced using the modeling techniques and software described in Sterne et al. (2011). In the top panel, the pattern is shown as a function of bearing angles. The gain pattern at several elevation angles is plotted. The Beam 7 maximum has a bearing of 21.48°, east of geographic north. Sidelobes in the immediate vicinity of this maximum are low – of the order of 10 dBi (decibels with respect to an isotropic radiator) below the maximum. However, the pattern does show a significant secondary maximum directed towards the southwest. This secondary must be considered when analyzing radar echo returns in SuperDARN data as some returns may arrive along this secondary maximum from behind the radar (cf. Milan et al., 1997b;

Burrell et al., 2015, 2018).

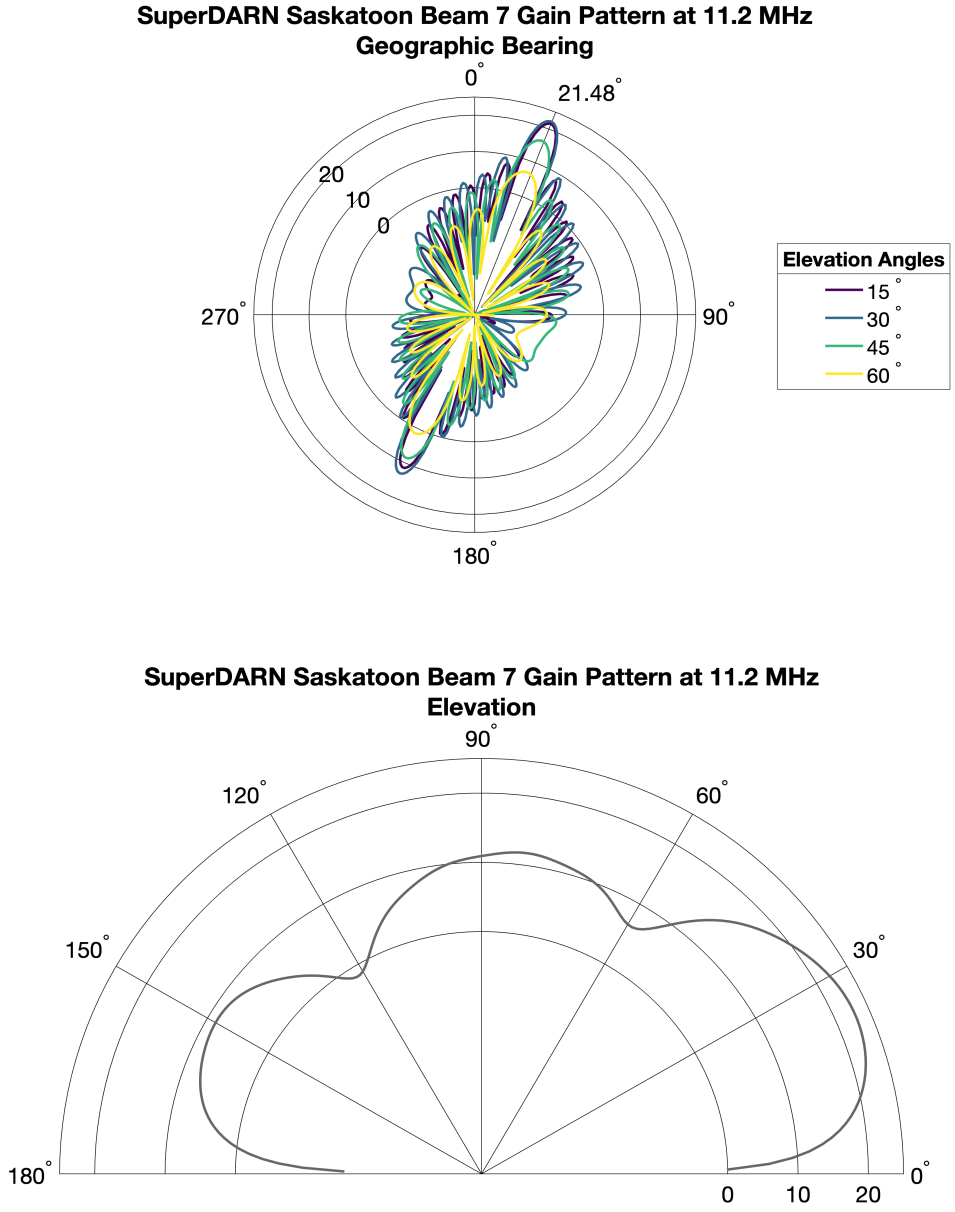

Figure 1. Polar plots of SuperDARN Saskatoon's Beam 7 gain pattern at 11.2 MHz, in dBi, as a function of geographic bearing at several elevation angles (top panel) and as a function of elevation along the bearing of 21.48° (bottom panel).

In the bottom panel, the gain pattern is plotted as a function of elevation angle along the bearing of Beam 7, showing a peak of approximately 22 dBi at 22° elevation with respect to the horizontal. In this work, we are only concerned with Beam 7 as it is considered the radar's central beam, and because it simplifies validation procedures when comparing signal power received by RRI when the targeted radar transmits on a solitary beam. The frequency of 11.2

MHz was chosen since it is a common frequency used for RRI experiments with SuperDARN Saskatoon. This frequency is also convenient since it is well enough above the expected plasma frequency of the region such that transmissions are easily detected by RRI while still exhibiting magnetoionic effects.

2.2 e-POP RRI

The Enhanced Polar Outflow Probe (e-POP) (Yau & James, 2015) is the science payload onboard CASSIOPE, which was launched into an 81° inclination, 325 × 1500 km orbit on September 29, 2013. Among e-POP's eight instruments is a digital radio receiver, RRI, whose scientific objectives include studying naturally and artificially generated radio emissions, and ionospheric plasma density structures. RRI is well suited for studying radio wave propagation in the high frequency regime (HF; 3-30 MHz) of the radio spectrum and is a significant advancement in HF radio science in the near-Earth geospace environment (Burrell, 2017). Since the start of e-POP's science operations, RRI has conducted several conjunctive experiments with SuperDARN radars, including the systems located at Saskatoon and Rankin Inlet.

SuperDARN radars are an ideal HF source for radio science experiments with RRI. The radars are distributed throughout the mid- to high-latitudes in both hemispheres; their operating band, 8-20 MHz, is almost entirely covered by RRI's operating range (10 Hz-18 MHz); and, conducting RRI experiments with SuperDARN is straightforward. Indeed, coordinated RRI and SuperDARN experiments have been the focus of, or featured in, several radio science experiments (e.g., Burrell et al., 2015, 2018; Perry et al., 2017).

2.3 PHaRLAP

The power profile of the SuperDARN Saskatoon radar will be propagated into the terrestrial ionosphere using the Pharlap ray tracing toolbox (Cervera and Harris, 2014). In this work, we use Pharlap's 3D ray tracing functionality, specifically, the *raytrace_3d_sp.m* method in Pharlap version 4.3, which provides a variety of important radio science parameters at regular points along each simulated ray including geographic location, phase path, refractive index, the angle between the ray normal and the geomagnetic field, the geometric distance traveled by the ray, and polarization information. Pharlap handles both the ordinary and extraordinary component of the HF rays separately. The software propagates individual HF rays from the launch point through an IRI ionosphere and international geomagnetic reference field (IGRF; Thébault et al., 2015), both of which can be easily modified or replaced by an alternative empirical model.

2.4 SuperDARN Saskatoon Power Density Profile Modeling Procedure

The main product of the model presented here is a power density map of the SuperDARN Saskatoon radar's radio emissions, gridded by geographic latitude, longitude, and altitude. These maps are constructed by superposing the power density contributions of each simulated ray that intersects a given bin. The power density, $\mathrm{P}(r)$, as a function of geometric range, *r*, for a given ray is:

$$\mathrm{P}(r) = \frac{P_T G(\theta, \phi)}{4\pi r^2} - P_{abs}(r) \qquad (1)$$

where P_T is the power of the radar's transmitter, $G(\theta, \phi)$, is the gain of the transmitter as a function of elevation angle θ and bearing ϕ as illustrated by Figure 1, and the nominal transmitting power of the radar (P_T) is provided by the University of Saskatchewan SuperDARN engineering team. The transmitter gain pattern $G(\theta, \phi)$ is modeled with the same software and techniques used by Sterne et al., (2011). The geometric range, r, is a Pharlap output product, calculated for each simulated ray. Lastly, $P_{abs}(r)$ accounts for the cumulative absorption calculated along a given ray path, described in Pederick & Cervera (2014).

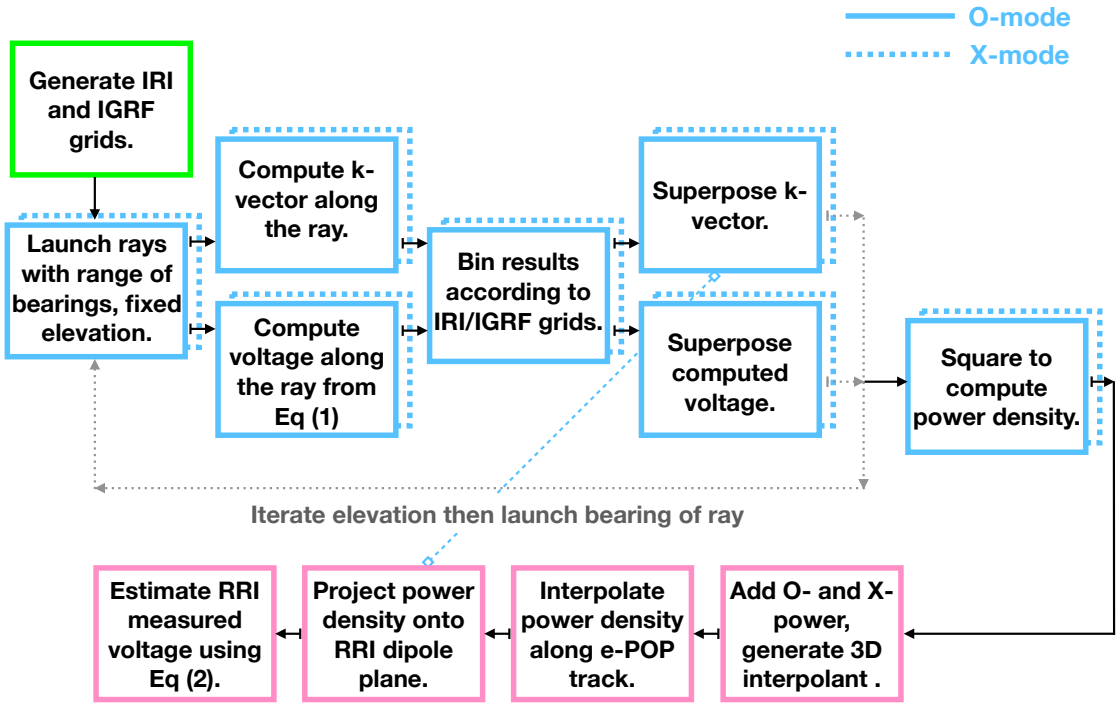

Figure 2. A flowchart describing the procedure for modeling the power density profile of the SuperDARN Saskatoon radar system, transmitting on Beam 7 at 11.2 MHz. Generating the IRI and IGRF grids is shown in green, computing the power density profile is shown in blue, and the validation procedure is shown in magenta.

Figure 2 is a flowchart describing the procedure for computing a power density profile for the SuperDARN Saskatoon radar at 11.2 MHz. First, for a specified moment in time, a three-dimensional grid of plasma density and magnetic field values is generated with separate calls to IRI and IGRF Pharlap functions (highlighted in green in Figure 2). For the results presented here, the grid spans 30°-80° N in geographic latitude and 155°-55° W in longitude with a resolution of 0.25°, and 50-1550 km in altitude with a 7.25 km resolution. This grid size and resolution were chosen to meet a desired resolution of the power density maps and encompass a significant portion of SuperDARN Saskatoon's field-of-view and CASSIOPE's altitude range. In calling IRI, we used an R12 value (12-month running average sunspot number) of 15, consistent with the conditions during the RRI's measurements which we will use for validation. Otherwise, the default settings encoded into Pharlap were used; the IRI 2012 model using the bottomside profile introduced by Bilitza et al. (2000) and the D-region model developed for IRI-1990.

After generating the IRI and IGRF grids, 11.2 MHz rays are then launched over a range of bearing angles at a fixed elevation angle. As Figure 2 illustrates, the power density map computation procedure iterates through a range of bearing (0°-360°) and elevation (10°-90°) angles, with a resolution of 0.10°. Equation 1 is calculated at points along each ray, in a step size no greater than 10 km. As previously discussed, the values for P_T and $G(\theta, \phi)$ are known a priori, while the value of geometric range, r, and cumulative absorption $P_{abs}(r)$ are provided as an output of the ray tracing software. Meanwhile, the unit k-vector for the wavevector is computed for each step size along the ray. The power and k-vector information are then binned in the same grids as the ionosphere and magnetic field data.

Pharlap provides a phase path estimate for each ray, which is used to calculate the instantaneous phase at any point along the rays in each bin. A wavevector is then constructed from this phase information, the square root of Equation 1 (a quantity proportional to an electric potential), and the aforementioned k-vector calculation so that multiple rays within a bin may be superposed. As the gray arrows in Figure 2 indicate, this process is iterated several times to account for all the desired rays.

The final gridded superposed electric potential values are then squared, producing a three-dimensional grid containing power density values and entries. This entire process, highlighted in blue in Figure 2, is computed separately for the O- and X-modes. Unlike the model in Gillies et al. (2010), the model presented here does not consider the initial polarization state of the transmitted rays at the radar; rather, the initial transmitting power is distributed evenly to each mode. We regard the Gillies et al. (2010) work as a higher-order correction that will be implemented in future versions of the model.

3 Results and validation

3.1 August 5, 2017 18:35 UT ray tracing example

Figure 3 shows Pharlap ray tracing results for August 5, 2017 at 18:35 UT. This time was specifically chosen as it coincides with an RRI experiment that will be discussed in more detail shortly. The top panel shows O- and X-mode rays originating from Saskatoon, Canada, launched along Beam 7's bearing, between from 10° and 90° in elevation angle, in 1° increments. For clarity, a reduced number of rays are plotted in Figure 3 compared to the modeling results that will be shown shortly, which consists of more rays.

A contour plot of plasma densities generated by IRI along the Saskatoon geographic meridian is also plotted in the background. CASSIOPE's tracks during the five conjunctions which will be used to validate the power density model are plotted in the foreground. A similar plot is shown in the bottom panel from a different vantage point. Here, only the paths of the rays launched at 30° elevation, from 0°-360° in bearing in 2° increments are shown between 50 and 500 km altitude. The contour plot in the background shows the IRI ionosphere at 245 km altitude.

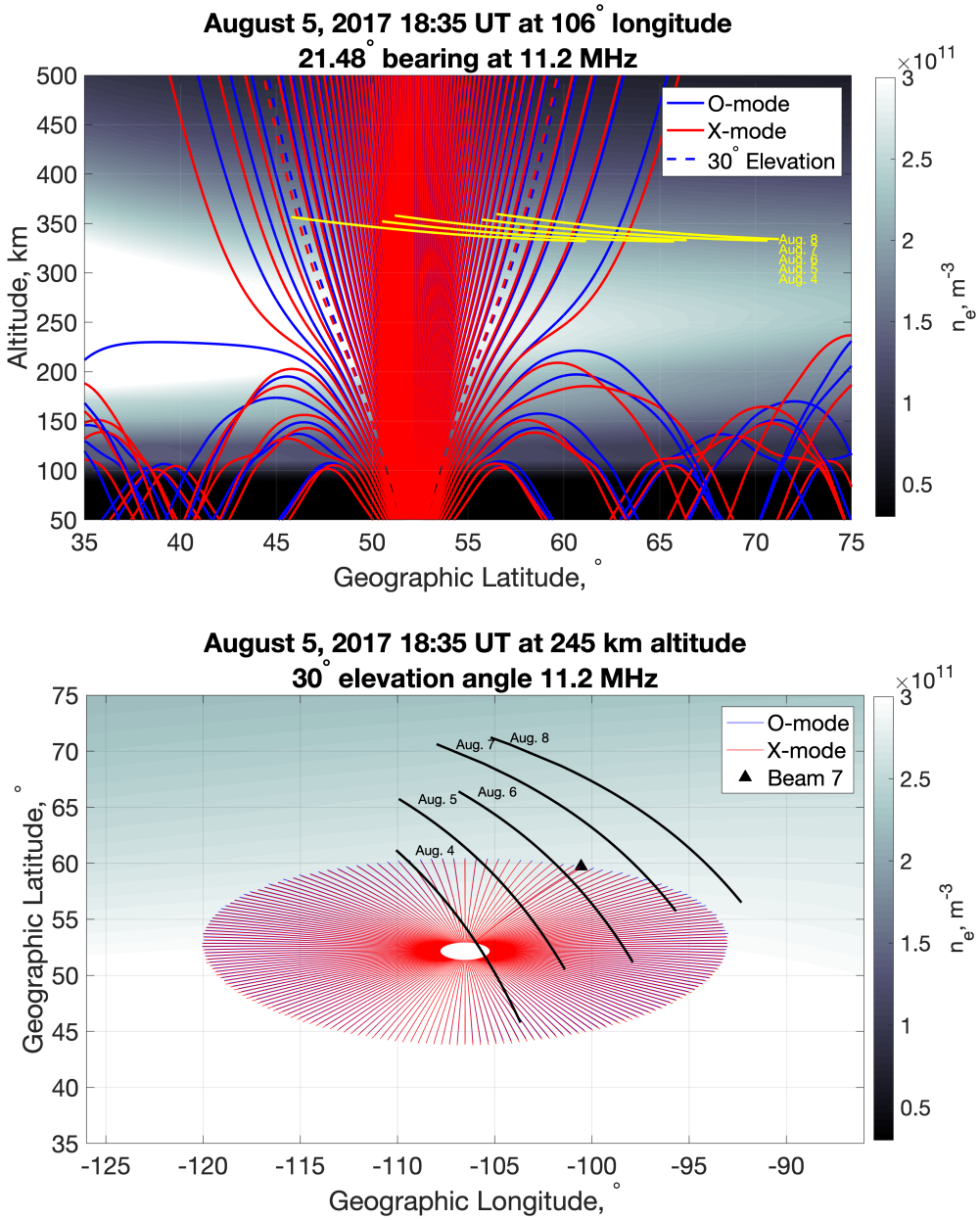

Figure 3. (top) Ray race simulation results for August 5, 2017 at 18:35 UT showing ray path for 11.2 MHz O- (blue) and X-mode (red) rays launched along front and rear facing maxima of the Beam 7 gain pattern as a function of geographic latitude and altitude at Saskatoon's longitude. Rays with a 30° elevation angle are indicated with dashed lines. (bottom) The same results but for rays launched at 30° elevation for all bearings, plotted as a function of geographic longitude and latitude at 245 km altitude. IRI plasma density contours are plotted in the background, with the CASSIOPE tracks of five RRI conjunctions plotted in the foreground. Rays along the Beam 7 bearing are indicated.

Both panels in Figure 3 show that the ray trace predicts that rays with elevation angles above ~25° can propagate directly through to the ionosphere, while rays at lower elevation angles are internally reflected and undergo multi-hop propagation without being able to propagate vertically

through the ionosphere downrange. A spacecraft in the region between 200 – 500 km altitude will only have access to the highest elevation rays shown in the bottom panel of Figure 3, according to the ray trace simulation.

3.2 August 5, 2017 18:35 UT power density map example

The main output of the SuperDARN power density model is a power density map of the radar's emissions in the vicinity of the radar. A map for August 5, 2017 at 18:35 UT is plotted in Figure

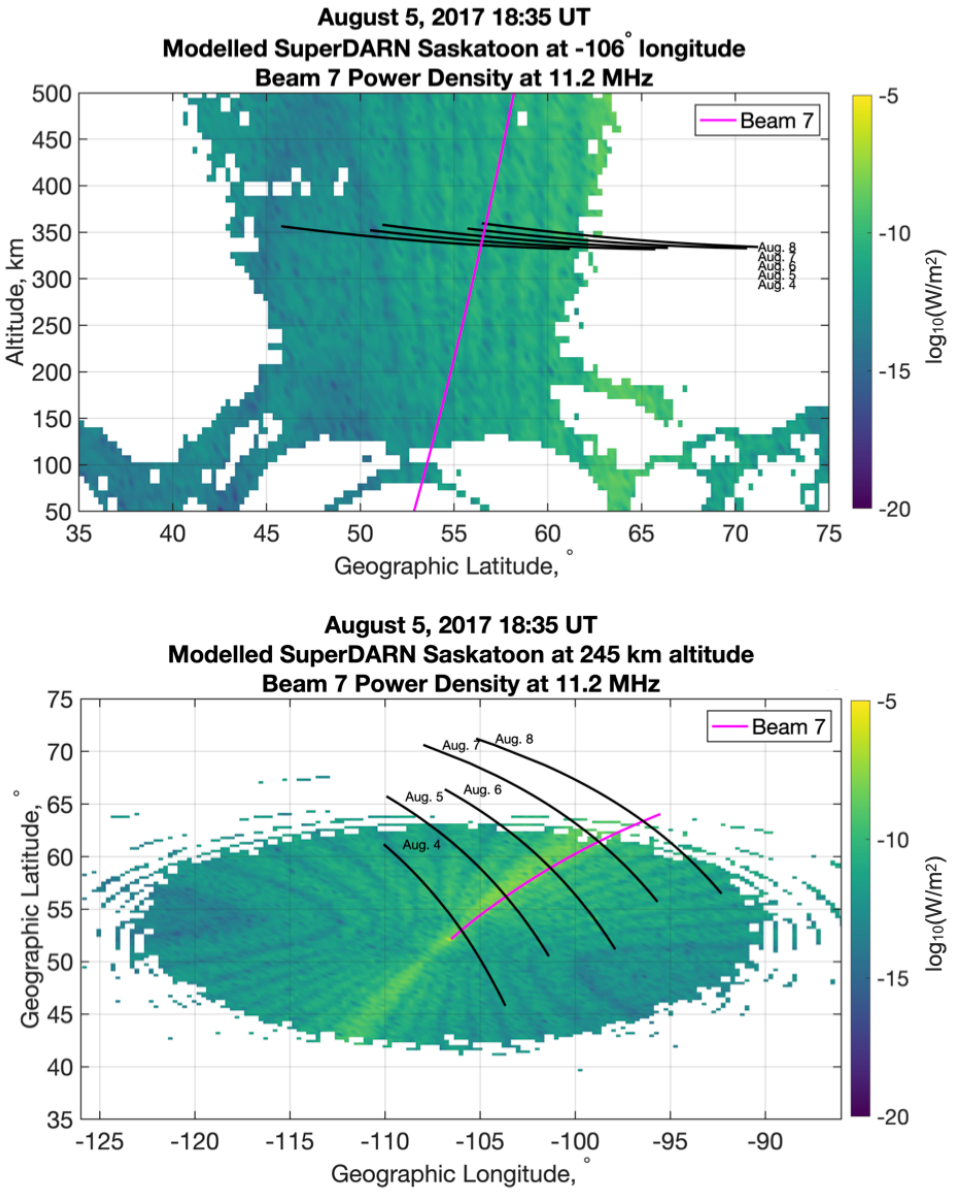

Figure 4. Simulated power density values plotted with the same axes in Figure 3. The nominal great-circle path along Beam 7's bearing is plotted in magenta in both plots. Beam 7's power density peak (bottom panel) in the front and back lobe is clear, as are the secondary peaks due to the sidelobes of the array's gain pattern (both panels).

4 with the same axes as Figure 3. This map combines contributions from the O and X propagation modes. Two clear differences between Figures 3 and 4 are that the latter shows binned power density values instead of ray paths, and that the elevation (top) and bearing (bottom) of Beam 7 are plotted in magenta.

The longitudinal slice (top panel, Figure 4) shows that, in the F region, the radar's radiated pattern is mostly constrained between 40 – 63° latitude. Below 200 km, the latitudinal range of the radar's radiated power is far more extensive, because of internal reflection, but it is much more intermittent. As the bottom panel of Figure 4 shows, the rays crate a geometric shape commonly referred to as the "iris of accessibility" (James, 2006). Within this region sub-orbital spacecraft such as sounding rocket payloads have access to the rays originating from the terrestrial transmitter.

The imprint of the radar array's gain pattern is readily apparent in the bottom panel of Figure 4, which shows the radar's power density at an altitude of 245 km. The peak forward radiated power is centered at approximately 19° in bearing, more northerly than the great-circle path trajectory of Beam 7 (21.48°). This is because the gain pattern (cf. Figure 1) for the higher elevation rays (>22° elevation) is directed more northerly. Lower elevation rays are internally reflected. The peak in the radar's back lobe is also clearly defined, which, as discussed earlier, must be considered when interpreting SuperDARN radar echo returns. Both top and bottom panels of Figure 4 also show modulations in power density. These are attributed to gain pattern's sidelobes.

In general, the modeling results displayed in Figure 4 are consistent with a general intuition of SuperDARN Saskatoon's power density profile. The power density peak is essentially aligned with the bearing of the transmitting beam (Beam 7 in Figure 4), constrained to a width of a few degrees bearing, and it is several factors stronger than the radar's sidelobes. Below approximately 200 km altitude, there is an absence of power density within a few hundred kilometers of the radar – the "skip zone". Above 200 km, the radiated power density is contained within the iris of accessibility. Power density maps for August 4, 6, 7 and 8, 2017, are provided in Supplementary Information as Figures S1 – S4, respectively.

3.3 Comparison to August 4 – 8, 2017 RRI conjunctions

We now turn our focus to validating the power density model by comparing its output to measurements collected during five experiments with RRI and SuperDARN Saskatoon, conducted between August 4 and August 8, 2017. In each experiment, the radar transmitted at 11.2 MHz along Beam 7. RRI was activated for 237 seconds starting at 18:57:14 UT on August 4, and approximately 23-24 minutes earlier each successive day as a result of CASSIOPE's nodal precession. RRI was tuned to 11.205 MHz and operated in the crossed-dipole mode (Perry et al., 2017). CASSIOPE's tracks for the five experiments are depicted with black traces in Figure 4. Except for the August 4 experiment, when the normal of RRI's dipole plane is along the spacecraft ram direction in the horizontal plane, CASSIOPE's attitude was slewed such that the normal of RRI's dipole plane was continuously directed at Saskatoon.

The procedure for validating the modeled power density profile is outlined in magenta in Figure 2. The end product of the procedure is a prediction of the total voltage measured by RRI's two

dipoles. First, a 3D interpolant of the power density profile of the radar is generated with dimensions of geographic latitude, longitude, and altitude. MATLAB's *scatteredInterpolant* function with a linear interpolation method was used for the results presented here.

The interpolant is then sampled at points along CASSIOPE's track, producing an estimate of the power density incident on RRI along the track. This estimate is then projected onto RRI's dipole plane by computing the dot product of the wave vector associated with the modeled power density value and the unit vector normal to RRI's dipole plane. Recall that the wave vector quantity was computed and stored during the ray tracing procedure (cf. Figure 2). The normal of RRI's dipole plane is calculated from CASSIOPE's attitude information contained in its ephemeris file.

The predicted RRI voltage, V, is then calculated using (Griffiths, 1999):

$$V = \sqrt{\frac{2 I L_{eff}^2}{n^2 \epsilon_0 c}} \qquad (2)$$

in which L_{eff} is the effective length of an RRI dipole antenna: 3 m (James, 2003), I is the power density projected onto RRI's dipole plane, n, is the index of refraction, provided by IRI at the spacecraft position, ϵ_0, is the permittivity of free space, and c, is the speed of light in a vacuum.

The predicted voltage, V, is then compared to the measured voltage of the radar pulses received by RRI. SuperDARN pulses were extracted from RRI's data using techniques described in Perry et al., (2017). The voltage measured by both dipoles at the midpoint of the detected pulse was added, then compared to the predicted voltage. Since RRI's dipoles are orthogonal to one another, the total voltage induced by the electromagnetic energy incident on RRI's plane can be computed by applying the Pythagorean theorem to the dipole voltages.

Figure 5 illustrates the results of the predicted RRI voltages (black) plotted together with the measured RRI voltages (red) as a function of CASSIOPE'e geographic latitude for the (a-e) August 4-8, 2017 experiments. The same results are plotted as a function of geographic longitude in Figure 6. In both plots, a 100-point moving median, equivalent to approximately 15 km distance along CASSIOPE's track, has been applied to the RRI data trace. Note that both axis in the different panels of each plot have different scales and ranges in general, in order to optimize the data display in each case. The magenta-colored vertical dashed line in both figures marks the point at which e-POP crosses the great-circle path of Beam 7's bearing – the same magenta line plotted in Figure 4 (both panels).

For the August 5 – 7 experiments, the modeled voltages values show good agreement with the measured values. The difference in predicted and measured peak voltages are within approximately 20%. The predicted voltage peaks are within about 2-3° in latitude (Figure 5) and 1-3° in longitude (Figure 6) of the measured values. The August 5 experiment shows the best agreement; the predicted voltage profile is nearly identical to the measured RRI voltages.

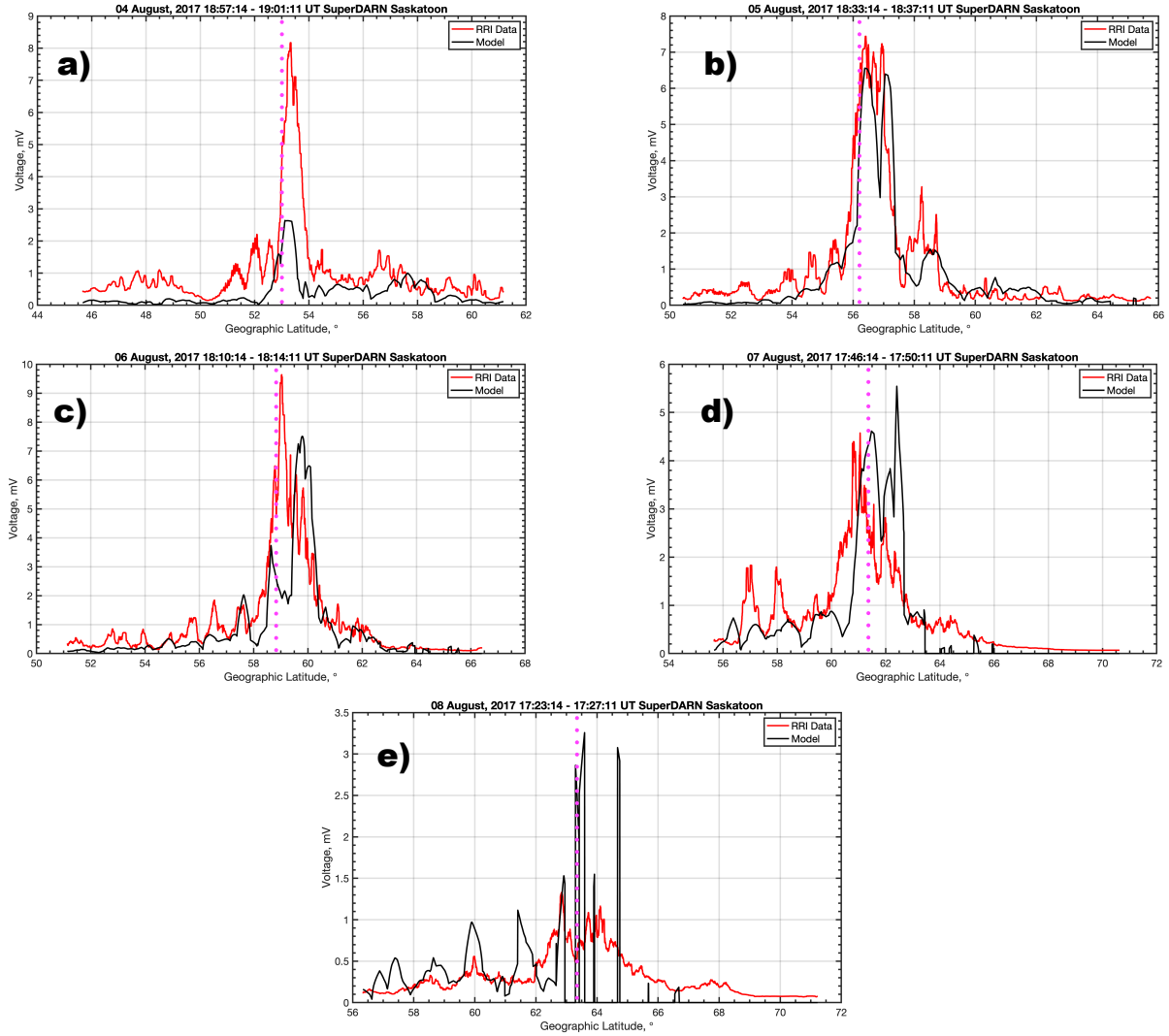

Figure 5. Predicted (black) and measured (red) RRI voltages as a function of geographic latitude for (a-e) August 4 – 8, 2017 RRI measurements of SuperDARN Saskatoon. Note that the different panels have different axis scales and/or ranges. The magenta-colored vertical dashed line marks the point at which e-POP crosses the great-circle path of Beam 7's bearing.

A persistent feature of note in the predicted August 4 – 7 voltage profiles is a double-hump maximum. A closer inspection of the model output reveals that each is due to a separation in the O- and X-mode power density profiles, in which the peaks located at higher latitudes are due to the O-mode. The double-hump feature is not observed in the RRI voltage profiles. The feature arises in the model because we have assumed that the transmitting power of the radar is distributed equally to O- and X-mode of propagation. According to Gillies et al., (2010), the initial transmitting power should be weighted towards the X-mode because of the radar's orientation with respect to the geomagnetic field. In reality less O-mode power should be expected at RRI's altitude, which would be reflected in the model output as a reduction in the amplitude of the higher-latitude hump. As mentioned earlier, the initial polarization at the radar site will be accounted for in future versions of the model.

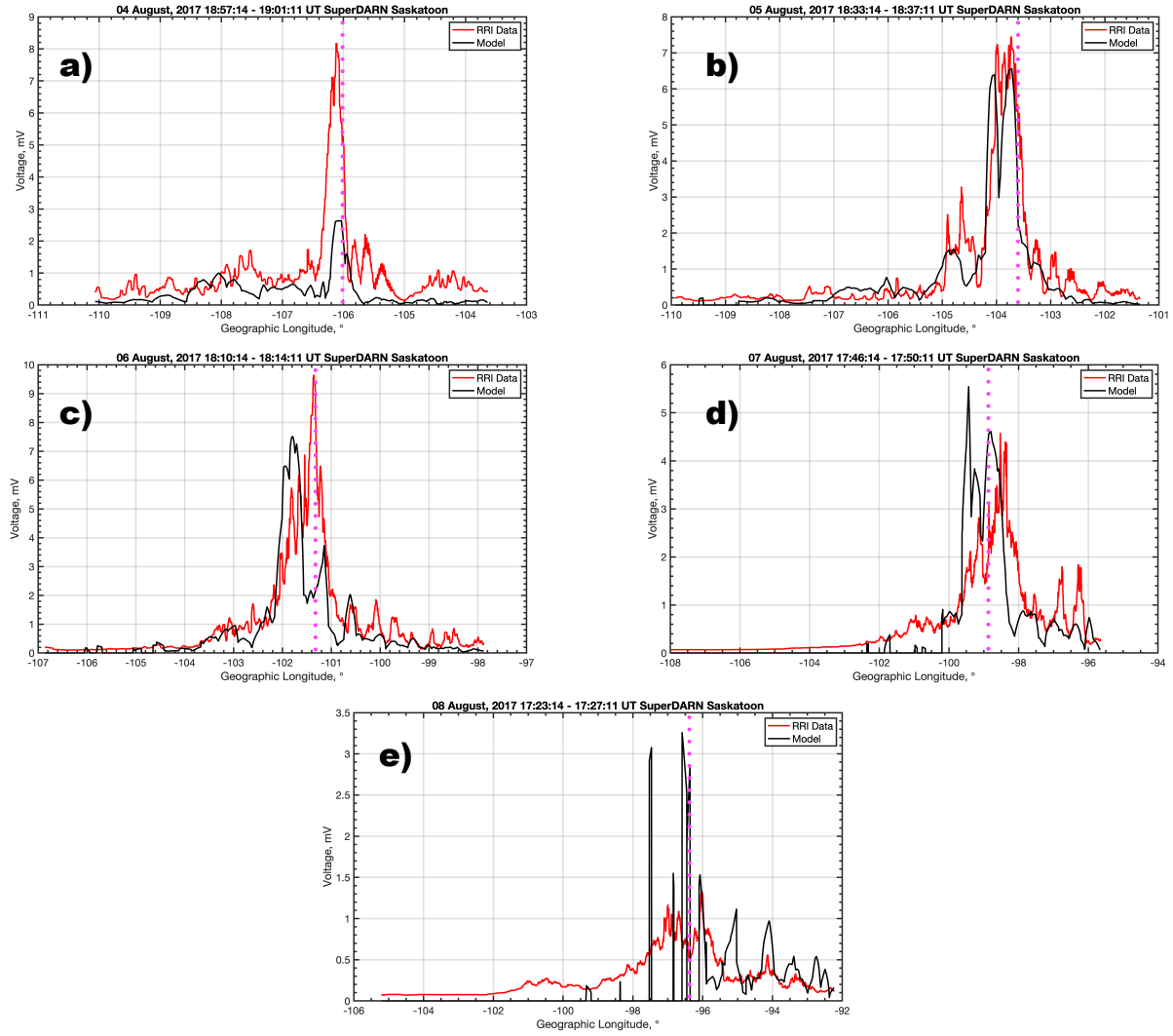

Figure 6. Predicted (black) and measured (red) RRI voltages as a function of geographic longitude for (a-e) August 4 – 8, 2017 RRI measurements of SuperDARN Saskatoon. Note that the different panels have different scales and/or ranges.

The measured voltage peaks differed from where e-POP crossed Beam 7's great-circle path by 0.5° in latitude and approximately the same amount in longitude. As Figures 5 and 6 show, the assumption that the radar's maximum power density lies along the great-circle path is reasonable for the August 4-8 experiments.

The August 4 and 8 experiments show considerable disagreement between the predicted and measured RRI voltages. For the August 4 experiment, the predicted voltage peak value is considerably lower than the measured peak value; however, there is good agreement on the location of the peak. Recall that for the August 4 experiment, CASSIOPE was unable to slew RRI towards SuperDARN Saskatoon, unlike the August 5-8 experiments. As the separation distance decreased, the angle between the line-of-sight to Saskatoon from CASSIOPE and the normal to RRI's dipole plane became more oblique. The result of this was an underestimation of RRI's effective area, L_{eff}^2.

The model assumes that L_{eff}^2 decreases like $|cos\,\theta|$, where θ is the angle between the wave vector of the incident radio wave and the normal to RRI's dipole plane. In reality, the relationship between L_{eff}^2 and an incident radio wave is much more complicated, especially when θ is in the vicinity of 90° (James, 2003). This is not accounted for in the validation procedure, and results in an underestimate of L_{eff}^2. This is the case for the August 4 pass when CASSIOPE is within a few degrees of latitude and longitude with respect to Saskatoon (52.16° N, 106.53° W, geographic).

There is clear disagreement between the model and RRI's measurements for the August 8 conjunction as well (cf. Figures 5 and 6). The model predicts sporadic and very low RRI voltage measurements, whereas RRI measured a subdued voltage profile. As Figure 4 shows, RRI's track during the August 8 experiment was mostly outside of the iris of accessibility, hence the predicted absence of RRI voltages. Overall, the measured RRI voltages are subdued and distorted compared to the previous days' measurements: there are two peaks rather than a singular peak, and the relative height of the peak is low compared to the previous conjunctions.

We attributed the August 8 disagreement to an overestimation of the ionospheric plasma density by IRI. A denser ionosphere would result in a more contracted iris of accessibility than what was encountered by RRI, which is reflected by the lack of predicted RRI voltages. A more tenuous ionosphere would have expanded the predicted iris of accessibility and would have likely generated a more accurate prediction of what RRI measured. We discuss this further in the discussion section.

Figure 7 provides a summary of the August 4 – 8 measurements of SuperDARN Saskatoon in a similar format to the top panel of Figure 1. Along with the Beam 7 gain pattern, the measured RRI voltages (normalized to 25 dB in gain value) are plotted as a function of bearing (top panel) with respect to the radar. This figure illustrates that, indeed, the relative voltage profile as a function of bearing is generally consistent with the modeled gain pattern. The peak measured voltages are aligned with the modeled gain pattern; the widths of the voltage peaks are also consistent with the model; and the sidelobes are reduced. As discussed earlier, the largest deviation between model and measurement occurred during the August 4 and 8 experiments, and there is a slight northward deviation in the peak measured voltage that is especially evident during the August 5 conjunction.

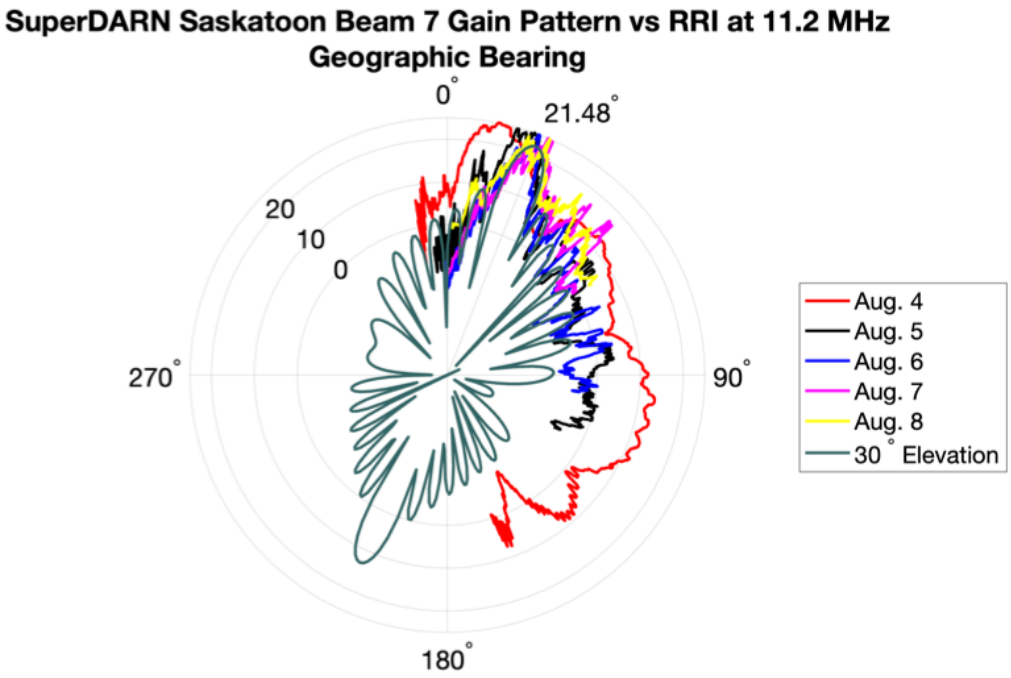

Figure 7. Summary of RRI's measurements of SuperDARN Saskatoon collected between August 4 – 8, 2017, plotted alongside the radar's modeled gain pattern, in the same format as the top panel in Figure 1.

4 Discussion

We have developed a model of the SuperDARN Saskatoon's radar's power density profile that accounts for HF radio wave propagation characteristics and extends into the F-region ionosphere. We have also compared the model with measurements of the radar's transmissions using RRI during five conjunctions that occurred between August 4 and 8, 2017. The measurements collected between August 5-7 show very good agreement with the model, while the August 4 and 8 measurements do not.

To the best of our knowledge, the model is unique in that it is the first and only to consider SuperDARN's power density profile at ionospheric altitudes. Knowledge of this quantity is critical to interpreting radar data as it indicates where the transmitter's power is directed and thus the likely location of the scattering volume. The strong agreement between the model and RRI's measurement on August 5-7 is a positive indication that the model is both accurate and a useful tool for understanding SuperDARN backscatter and interpreting RRI's measurements of the system.

4.1 Model limitations

It is important to note that the model does have its limitations. First, it only considers transmissions at 11.2 MHz, which is at the approximate midpoint of the radar's usual transmitting range of 10 – 12 MHz. Future development of the model will include a more extensive range of transmitting frequencies used by the radar. Additionally, the power density

514 profile is exclusive to SuperDARN Saskatoon's array of log-periodic antennas. It would not be
515 appropriate to apply the model to another radar of different construction, for example, the
516 SuperDARN radar located at Rankin Inlet, Canada, which is made-up of twin terminated folded
517 dipole antennas (Sterne et al., 2011).
518
519 We have validated the model during daytime conditions under generally calm geomagnetic
520 conditions. The Kp index was 3, 3, 2, 0, and 2 during the August 4-8 conjunctions, respectively.
521 The accuracy of the model during nighttime and/or more disturbed conditions will be
522 investigated in future studies. It is expected that the model will have greater difficulty making
523 accurate predictions under more disturbed conditions since SuperDARN Saskatoon's nominal
524 field-of-view intersects with the auroral oval where plasma density irregularities are frequent.
525 With respect to nighttime under calm geomagnetic conditions, we anticipate good agreement
526 given that the HF rays will be less affected by the depleted ionospheric density and absorption.
527
528 The model is also limited by its reliance on IRI as an empirical ionosphere. This means that the
529 power density profile model may only be accurate in a statistical sense and is likely not as
530 applicable during geomagnetically disturbed conditions or when transient phenomena are
531 present, such as auroral precipitation. The ionosphere's day-to-day variability is extremely
532 difficult to replicate with an empirical model. Indeed, IRI has been shown to be deficient in the
533 Canadian sector in general (Themens et al., 2017). Future developments of the model will
534 replace IRI with the Empirical Canadian High Arctic Ionospheric Model (E-CHAIM; Themens
535 et al., 2017) which has been shown to be more suitable for the region.

536 ### 4.2 The August 8, 2017 conjunction

537 The lack of agreement between the modeled predictions and RRI measurements during the
538 August 8 conjunction is likely a consequence of IRI's constraints. As discussed earlier, we
539 hypothesize that the discrepancy is a result of IRI overestimating ionospheric density, resulting
540 in a more contracted iris of accessibility than what RRI encountered on August 8. To explore
541 this hypothesis further, we have plotted the SuperDARN backscatter data from the August 4-8
542 conjunctions in Figure 8, generated using the pyDARNio software package (version 1.0; The
543 SuperDARN Data Analysis Working Group, 2021) which shows a plot of the time averaged
544 backscatter power (Signal to Noise Ratio; SNR) measured during the conjunctions. The
545 geographic latitude of the echoes was computed using the Chisham et al., (2008) virtual height
546 model.
547
548 The northward movement of the scatter on August 8 (yellow trace) compared to the previous
549 days is indicative of a more tenuous ionosphere on that day, which would result in an expanded
550 iris of accessibility. This movement is especially evident north of 60°. It is challenging to
551 distinguish ionospheric and ground scatter in the radar echo data presented in Figure 8. Figure 3
552 indicates that both may be present. In either case, the scattering locations of both are expected to
553 move north as the density of the intervening ionosphere decreases since the HF rays will undergo
554 less refraction and will require a longer path length to satisfy the aspect angle condition or
555 backscatter off the ground. This corroborates the hypothesis that the disparity between
556 prediction and measurements on August 8 was due to IRI's overestimation of the ionospheric
557 density, whereas IRI's prediction for August 4-7 was more accurate.

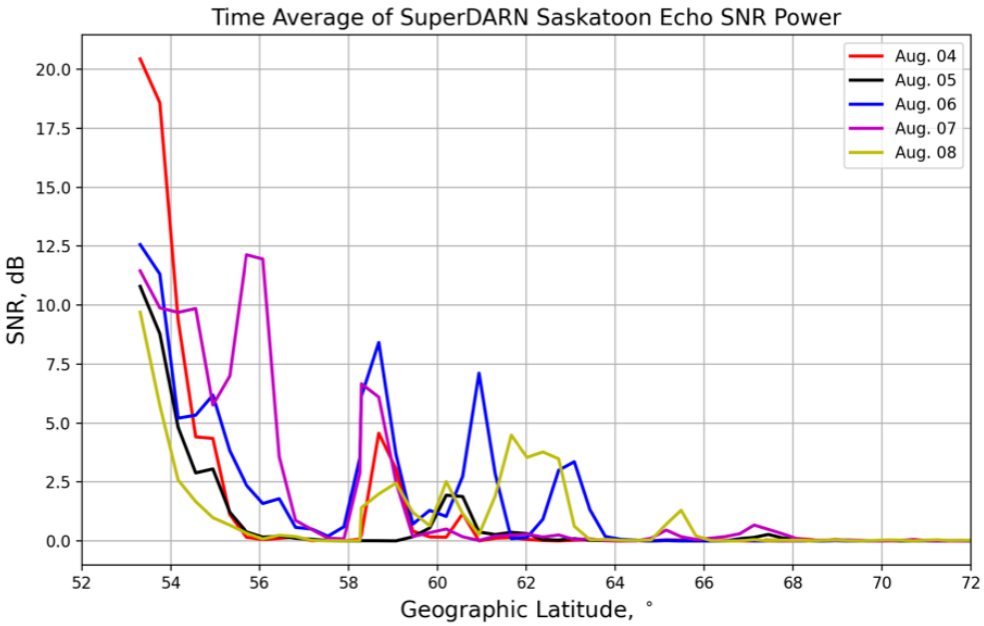

Figure 8. Time average of SuperDARN Saskatoon backscatter power (signal-to-noise ratio; SNR) as a function of geographic latitude, collected by Beam 7 during the RRI experiments August 4 – 8, 2017.

4.3 Response to more intense solar conditions

We also investigated the model's response to a variety of solar conditions. Different IRI ionospheres were compared, with the goal of better understanding the variability of the modeled power density profile. In particular, an IRI ionosphere with driving R12 values of 60 and 100 were used (an R12 of 15 was used in modeling the August 4-8 experiments), consistent with much more intense solar activity. The only effect the higher R12 values had was to decrease the peak predicted RRI voltage (not shown) and contract the iris of accessibility. The locations of the voltage peaks were moved slightly southward, consistent with a denser ionosphere.

4.4 Relevance to SuperDARN and HF radio science

The model has important implications for remote sensing the MIT system, which can be used to improve the interpretation of SuperDARN data and in particular the SuperDARN geolocation algorithms. Unlike determining whether radar echoes originate from in front of or behind the radar, which can be accomplished with SuperDARN's interferometry data (e.g., Milan et al., 1997b; Burrell et al., 2015, 2018), it is unlikely that a comprehensive method of measuring the effective pointing direction of the radar's transmitting beam is feasible based solely on the radar's data.

Models of SuperDARN's power density profile, like the one presented and validated in this work, are a helpful tool for enhancing SuperDARN data analysis and improving our understanding of HF radio wave propagation characteristics in the high-latitude regions. For example, the model can be used to simulate SuperDARN Saskatoon backscatter echoes by considering the power density profile of the radar in addition to where the aspect angle condition

is satisfied in the radar's field-of-view. The simulated echoes can then be used as a guide for interpreting backscatter data in terms of both occurrence and echo power. This new capability is an advance on traditional SuperDARN modeling which, in general, has not accounted for the power density profile of the system.

SuperDARN data products assume that the scattering volume for a corresponding radar echo is located along a great-circle path of the transmitting beam's bearing. As Figures 5-7 demonstrate, this assumption is reasonably accurate under quiet geomagnetic conditions. The effective pointing direction of SuperDARN Saskatoon's Beam 7, as measured by RRI, is of the order of 0.5° in latitude and longitude deviated from the beam's nominal great-circle path. This is a negligible amount in lateral deviation – it amounts to a fraction of a beamwidth, but it is approximately equivalent to a SuperDARN range gate in group delay – 45 km, a value that is consistent with the expected SuperDARN echo geolocation accuracy (Yeoman et al., 2008). It seems plausible, then, that the indeterminacy of the transmitting beam's main lobe at ionospheric altitudes is an important, yet underappreciated, contributor to the error in SuperDARN's geolocation methodology.

Little is known about the stability of the transmitting beam under more disturbed geomagnetic conditions or more regular events such as when the day/night terminator intersects with the beam, or how such perturbations might influence the data. At polar latitudes, there is strong evidence that the transmitting beam undergoes significant deviations (Perry et al., 2016), which is consistent with other radio experiments in the polar region (Warrington et al., 1997). In both cases, polar-cap patches were identified as the likely cause of the deviations. Even though the lateral plasma density gradients that are common in the polar-cap region are rarely observed at lower latitudes, it is still conceivable that transmitting beam deviations may occur with other SuperDARN radars, such as the Saskatoon radar, which may have a non-negligible effect on the accuracy radar echo geolocation.

5 Summary

We have developed a novel model of SuperDARN Saskatoon's power density profile at ionospheric altitudes. The model advances on previous SuperDARN and HF radio wave propagation modeling in that it accounts for the ionospheric medium and its influence on HF radio wave propagation and quantifies the power density profile of the radar system at ionospheric altitudes. We have validated the model using RRI measurements collected between August 4-8, 2017. The model's predictions are in good agreement with RRI's measurements, demonstrating that the model is useful for predicting a SuperDARN radar's power density profile, provided the appropriate gain pattern for the radar is used.

The model is a tool for interpreting SuperDARN backscatter data as it provides a method for locating the scattering volume based on the radar's power profile, which supplements the traditional method of determining where the aspect angle condition is satisfied in the radar's field-of-view. It can also be used as a tool for interpreting RRI measurements of SuperDARN transmissions and other ground-based transmitters; one simply needs to apply the appropriate gain pattern for the targeted HF transmitter. Future developments of the model include expanding the model to consider other SuperDARN transmitting frequencies and an alternate empirical ionosphere.

Acknowledgments, Samples, and Data

This work was carried-out by KDR for an undergraduate project at the University of Calgary under the supervision of GWP and AWY. The authors thank Dr. Kathryn McWilliams and the SuperDARN Canada engineering team for facilitating RRI's measurements. The authors also thank Dr. Glenn Hussey and Clifford Ridley for their informative discussions and advice. Finally, the authors are indebted to the members of the e-POP Science Operations Centre, without whom RRI's measurements would not be possible.

We acknowledge funding support from the Canadian Space Agency under Grant 16SUSTSSPI, Natural Sciences and Engineering Research Council of Canada under Discovery Grant RGPIN/06069-2014 to AWY and the European Space Agency (ESA) Third Party Mission Program.

The power density profile model code may be accessed at GWP's github page: https://github.com/GWPerryNJIT. The results published in this paper were obtained using the HF propagation toolbox, PHaRLAP, created by Dr. Manuel Cervera, Defence Science and Technology Group, Australia (manuel.cervera@dst.defence.gov.au). This toolbox is available by request from its author.

The authors acknowledge the use of data from SuperDARN, an international project made possible by the national funding agencies of Australia, Canada, China, France, Italy, Japan, South Africa, Norway, the United Kingdom and the United States of America. SuperDARN data can be downloaded from Globus, instructions of which are provided here: https://superdarn.ca/data-products.

The RRI data used in this study are publicly accessible at: https://epop.phys.ucalgary.ca/data/. The Kp-index data used in this study is publicly accessible at: https://www.swpc.noaa.gov/products/planetary-k-index.

The authors also acknowledge the use of the *numpy* and *Scipy* packages.

References

André, R., Hanuise, C., Villain, J. P., & Cerisier, J. C. (1997). HF radars: Multifrequency study of refraction effects and localization of scattering. *Radio Science*, *32*(1), 153–168. https://doi.org/10.1029/96RS02987

Bilitza, D., Radicella, S. M., Reinisch, B. W., Adeniyi, J. O., Gonzalez, M. E. M., Zhang, S. R., & Obrou, O. (2000). New B0 and B1 models for IRI. *Advances in Space Research*, *25*(1), 89–95. https://doi.org/10.1016/S0273-1177(99)00902-3

Bilitza, D., & Reinisch, B. W. (2008). International Reference Ionosphere 2007: Improvements and new parameters. *Advances in Space Research*, *42*(4), 599–609. https://doi.org/10.1016/j.asr.2007.07.048

669 Bristow, W. A., Hampton, D. L., & Otto, A. (2016). High-spatial-resolution velocity
670 measurements derived using Local Divergence-Free Fitting of SuperDARN observations.
671 *Journal of Geophysical Research A: Space Physics*, *121*(2), 1349–1361.
672 https://doi.org/10.1002/2015JA021862

673 Burrell, A. G. (2017). e-POP RRI provides new opportunities for space-based, high-frequency
674 radio science experiments. *Radio Science*, *52*(4), 516–518.
675 https://doi.org/10.1002/2017RS006257

676 Burrell, A. G., Milan, S. E., Perry, G. W., Yeoman, T. K., & Lester, M. (2015). Automatically
677 determining the origin direction and propagation mode of high-frequency radar backscatter.
678 *Radio Science*, *50*(12), 1225–1245. https://doi.org/10.1002/2015RS005808

679 Burrell, A. G., Perry, G. W., Yeoman, T. K., Milan, S. E., & Stoneback, R. (2018). Solar
680 Influences on the Return Direction of High-Frequency Radar Backscatter. *Radio Science*.
681 https://doi.org/10.1002/2017RS006512

682 Cervera, M. A., & Harris, T. J. (2014). Modeling ionospheric disturbance features in quasi-
683 vertically incident ionograms using 3-D magnetoionic ray tracing and atmospheric gravity
684 waves. *Journal of Geophysical Research: Space Physics*, *119*(1), 431–440.
685 https://doi.org/0.1002/2013JA019247

686 Chisham, G., Lester, M., Milan, S. E., Freeman, M. P., Bristow, W. a., Grocott, A., … Walker,
687 A. D. M. (2007). A decade of the Super Dual Auroral Radar Network (SuperDARN):
688 scientific achievements, new techniques and future directions. *Surveys in Geophysics*, *28*(1),
689 33–109. https://doi.org/10.1007/s10712-007-9017-8

690 Chisham, G., Yeoman, T. K., & Sofko, G. J. (2008). Annales Geophysicae Mapping ionospheric
691 backscatter measured by the SuperDARN HF radars – Part 1: A new empirical virtual
692 height model. *Ann. Geophys*, *26*(4), 823–841. https://doi.org/10.5194/angeo-26-823-2008

693 Gillies, R. G., Hussey, G. C., Sofko, G. J., & James, H. G. (2010). Relative O- and X-mode
694 transmitted power from SuperDARN as it relates to the RRI instrument on ePOP. *Ann.*
695 *Geophys.*, *28*(3), 861–871. https://doi.org/10.5194/angeo-28-861-2010

696 Griffiths, D. J. (1999). *Introduction to Electrodynamics*, Upper Saddle River, New Jersey:
697 Prentice Hall.

698 James, H. G. (2003). High-frequency direction finding in space. *Review of Scientific Instruments*,
699 *74*(7), 3478. https://doi.org/10.1063/1.1581396

700 James, H. G. (2006). Effects on transionospheric HF propagation observed by ISIS at middle and
701 auroral latitudes. *Advances in Space Research*, *38*(11), 2303–2312.
702 https://doi.org/10.1016/j.asr.2005.03.114

James, H. G., King, E. P., White, A., Hum, R. H., Lunscher, W. H. H. L., & Siefring, C. L. (2015). The e-POP Radio Receiver Instrument on CASSIOPE. *Space Science Reviews*, *189*(1–4), 79–105. https://doi.org/10.1007/s11214-014-0130-y

Michael, C. M., Yeoman, T. K., Wright, D. M., Milan, S. E., & James, M. K. (2020). A Ray Tracing Simulation of HF Ionospheric Radar Performance at African Equatorial Latitudes. *Radio Science*, *55*(2). https://doi.org/10.1029/2019RS006936

Milan, S. E., Yeoman, T. K., Lester, M., Thomas, E. C., & Jones, T. B. (1997a). Initial backscatter occurrence statistics from the CUTLASS HF radars. *Annales Geophysicae*, *15*(6), 703–718. https://doi.org/10.1007/s00585-997-0703-0

Milan, S. E., Jones, T. B., Robinson, T. R., Thomas, E. C., & Yeoman, T. K. (1997b). Interferometric evidence for the observation of ground backscatter originating behind the CUTLASS coherent HF radars. *Ann. Geophys.*, *15*(1), 29–39. https://doi.org/10.1007/s00585-997-0029-y

Pederick, L. H., & Cervera, M. A. (2014). Semiempirical Model for Ionospheric Absorption based on the NRLMSISE-00 atmospheric model. *Radio Sci.*, (49), 81–93. https://doi.org/10.1002/2013RS005274

Perry, G. W., Miller, E. S., James, H. G., Howarth, A., St.-Maurice, J.-P, and Yau A. W. (2016). HF radar transmissions that deviate from great-circle paths: new insight from e-POP RRI. Paper presented at American Geophysical Union Fall Meeting, San Francisco, USA

Perry, G. W., James, H. G., Gillies, R. G., Howarth, A., Hussey, G. C., McWilliams, K. A., White, A., and Yau, A. W. (2017). First results of HF radio science with e-POP RRI and SuperDARN. *Radio Science*. https://doi.org/10.1002/2016RS006142

Ponomarenko, P. V., St-Maurice, J.-P., Waters, C. L., Gillies, R. G., & Koustov, A. V. (2009). Refractive index effects on the scatter volume location and Doppler velocity estimates of ionospheric HF backscatter echoes. *Annales Geophysicae*, *27*(11), 4207–4219. https://doi.org/10.5194/angeo-27-4207-2009

Ruohoniemi, J. M., Greenwald, R. A., Baker, K. B., Villain, J. P., & McCready, M. A. (1987). Drift motions of small-scale irregularities in the high-latitude F region: An experimental comparison with plasma drift motions. *Journal of Geophysical Research: Space Physics*, *92*(A5), 4553–4564. https://doi.org/10.1029/JA092iA05p04553

Ruohoniemi, J. M., & Baker, K. B. (1998). Large-scale imaging of high-latitude convection with Super Dual Auroral Radar Network HF radar observations. *Journal of Geophysical Research*, *103*(A9), 20797-- 20811. https://doi.org/10.1029/98JA01288

The SuperDARN Data Analysis Working Group (2021). *SuperDARN/pydarn: pyDARNio v2.0.1*. https://doi.org/10.5281/ZENODO.4558130

738 Sterne, K. T., Greenwald, R. A., Baker, J. B. H., & Ruohoniemi, J. M. (2011). Modeling of a
739 twin terminated folded dipole antenna for the Super Dual Auroral Radar Network
740 (SuperDARN). *2011 IEEE RadarCon (RADAR)*, 934–938. IEEE

741 Thébault, E., Finlay, C. C., Beggan, C. D., Alken, P., Aubert, J., Barrois, O., … Zvereva, T.
742 (2015). International Geomagnetic Reference Field: the 12th generation. *Earth, Planets and*
743 *Space*, *67*(1), 1–19. https://doi.org/10.1186/s40623-015-0228-9

744 Themens, D. R., Jayachandran, P. T., Galkin, I., & Hall, C. (2017). The Empirical Canadian
745 High Arctic Ionospheric Model (E-CHAIM): NmF2and hmF2. *Journal of Geophysical*
746 *Research: Space Physics*, *122*(8), 9015–9031. https://doi.org/10.1002/2017JA024398

747 Tsunoda, R. T. (1988). High-latitude F region irregularities: A review and synthesis. *Reviews of*
748 *Geophysics*, *26*(4), 719–760. https://doi.org/10.1029/RG026i004p00719

749 Villain, J. P., Caudal, G., & Hanuise, C. (1985). A Safari-Eiscat comparison between the velocity
750 of F region small-scale irregularities and the ion drift. *Journal of Geophysical Research:*
751 *Space Physics*, *90*(A9), 8433–8443. https://doi.org/10.1029/JA090iA09p08433

752 Warrington, E. M., Rogers, N. C., & Jones, T. B. (1997). Large HF bearing errors for
753 propagation paths contained within the polar cap. *IEE Proceedings: Microwaves, Antennas*
754 *and Propagation*, *144*(4), 241–249. https://doi.org/10.1049/ip-map:19971187

755 Warrington, E. M., Zaalov, N. Y., Naylor, J. S., & Stocker, A. J. (2012). HF propagation
756 modeling within the polar ionosphere. *Radio Science*, *47*(4).
757 https://doi.org/10.1029/2011RS004909

758 Yau, A. W., & James, H. G. (2015). CASSIOPE Enhanced Polar Outflow Probe (e-POP)
759 Mission Overview. *Space Science Reviews*, *189*(1–4), 3–14. https://doi.org/10.1007/s11214-
760 015-0135-1

761 Yeoman, T. K., Chisham, G., Baddeley, L. J., Dhillon, R. S., Karhunen, T. J. T., Robinson, T. R.,
762 … Wright, D. M. (2008). Mapping ionospheric backscatter measured by the SuperDARN
763 HF radars - Part 2: Assessing SuperDARN virtual height models. *Annales Geophysicae*,
764 *26*(4), 843–852. https://doi.org/10.5194/angeo-26-843-2008